Catalysis Science & Technology

PAPER

Cite this: *Catal. Sci. Technol.*, 2019, **9**, 5150

Purposefully designing novel hydroxylated and carbonylated melamine towards the synthesis of targeted porous oxygen-doped g-C_3N_4 nanosheets for highly enhanced photocatalytic hydrogen production†

Peng Song, Shuhua Liang,* Jie Cui, Dong Ren, Ruyan Duan, Qing Yang and Shaodong Sun *

Received 19th July 2019,
Accepted 23rd August 2019

DOI: 10.1039/c9cy01434a

rsc.li/catalysis

Graphitic carbon nitride (g-C_3N_4) has been considered as a promising metal-free photocatalyst, but the bulk still suffers from a low specific surface area and poor quantum efficiency. Exfoliation of the bulk into porous heteroatom-doped nanosheets has been confirmed to be an effective strategy for improving the photocatalytic activity. However, purposefully designing targeted precursors towards the synthesis of porous heteroatom-doped g-C_3N_4 nanostructures for enhanced photocatalytic activity is still a challenge. Here, we intentionally design and construct a new hydroxylated and carbonylated melamine precursor for preparing targeted porous O-doped g-C_3N_4 nanosheets based on the thermal polymerization reaction pathway. The as-prepared porous O-doped g-C_3N_4 nanosheets possess a high specific surface area which provides more active sites, and exhibit enhanced transfer and separation of charge carriers, thus displaying an about 18-fold higher hydrogen production activity than the bulk counterpart. This work would stimulate widespread investigations into the development of a designated precursor-reforming strategy for synthesizing highly-active g-C_3N_4 photocatalysts.

1. Introduction

As a consequence of aggravating environmental and energetic issues, photocatalysis with the advantages of mild reaction conditions and direct conversion of solar energy into chemical energy has attracted much more attention for producing clean and sustainable energy as well as alleviating the serious environmental pollution.[1,2] In particular, scientists are highly interested in photocatalytic hydrogen production due to its relatively low cost, easy implementation and high efficiency, making it the "21st century dream technology".[3,4] Therefore, it is significant to design and produce a highly efficient, stable and environmentally friendly photocatalyst.

Among the numerous types of photocatalysts, graphitic carbon nitride (g-C_3N_4), a two-dimensional (2D) visible light-driven, environment-friendly catalyst with excellent thermal and chemical stabilities, shows great potential in the fields of hydrogen evolution, degradation of organic pollutants and reduction of carbon dioxide (CO_2).[5–8] However, bulk g-C_3N_4 still suffers from few active sites, a high charge carrier recombination rate and limited visible-light utilization.[9] Therefore, some modification strategies have been developed to improve the photocatalytic performance of g-C_3N_4, such as exfoliation, morphology control, doping, heterojunction, and so on.[10–14] In particular, porous heteroatom-doped g-C_3N_4 nanosheets can not only enhance light harvesting and create more readily accessible channels for charge carrier transfer and more surface active sites for reaction, but also optimize the electronic structure, contributing to its stronger redox ability toward photocatalytic reactions.[15] For example, porous O-doped g-C_3N_4 nanosheets were synthesized by the

Shaanxi Province Key Laboratory for Electrical Materials and Infiltration Technology, School of Materials Science and Engineering, Xi'an University of Technology, Xi'an 710048, Shaanxi, People's Republic of China.
E-mail: liangsh@xaut.edu.cn, sdsun@xaut.edu.cn

† Electronic supplementary information (ESI) available: Schematic diagram of the formation mechanism of hydroxylated and carbonylated melamine. XRD patterns, FTIR spectra and TGA curves of the commercial MA, HCN-precursor and POCN-precursor. Solid-state ^{13}C MAS NMR of the HCN-precursor and POCN-precursor. N_2 adsorption/desorption isotherms and pore distributions of the CN, HCN and POCN samples. High-resolution O 1s spectra of CN, HCN, POCN-0.25, POCN-0.50, POCN and POCN-1.00. The geometry structure of O-doped g-C_3N_4 and DFT calculation results. XRD patterns, FTIR spectra and TEM images of the recycled POCN sample. Relative content of various nitrogen species of CN, HCN and POCN samples. The amount of the C–O bond derived from the high-resolution O 1s spectra of CN, HCN, POCN-0.25, POCN-0.50, POCN and POCN-1.00. Comparison of the photocatalytic hydrogen evolution performance of POCN with other recently reported g-C_3N_4. See DOI: 10.1039/c9cy01434a

precursor-reforming polymerization method,[16,17] which combined the advantages of exfoliation, porous structure and oxygen doping into the g-C_3N_4 framework to enhance the photocatalytic performance. Consequently, it is necessary to understand the roles of the different chemical structures of the precursor in the thermal polymerization reaction. Thus, the microstructure and composition of g-C_3N_4 would be rationally controlled by purposefully constructing functional precursors. Nevertheless, intentionally designing novel precursors towards the synthesis of porous heteroatom-doped g-C_3N_4 nanostructures for enhanced photocatalytic activity is still a challenge.

Herein, we purposefully design and construct a new hydroxylated and carbonylated melamine precursor for preparing targeted porous O-doped g-C_3N_4 nanosheets based on the thermal polymerization reaction pathway. During this process, the oxygen atom in anchored hydroxyl would be retained to contribute to oxygen doping, while an alternative oxygen atom in anchored carbonyl could be simultaneously removed in the form of water, resulting in the formation of porous nanostructures because of the mass loss of functional melamine. Thus, the integration of exfoliation, porous nanostructure and oxygen doping is simultaneously achieved in the g-C_3N_4 framework. The resultant products display a high specific surface area and enhanced transfer and separation of charge carriers. The photocatalytic hydrogen evolution rate (HER) of the as-prepared porous O-doped g-C_3N_4 (64.30 μmol h^{-1}) is 17.8 times higher than that of the bulk g-C_3N_4 (3.60 μmol h^{-1}), and the apparent quantum efficiency (AQE) at 420 nm reaches about 12.06%. This strategy might give rise to a promising new stream of thoughts to design and synthesize highly efficient porous heteroatom-doped g-C_3N_4 nanosheets.

2. Experimental section

2.1 Chemicals

All the reagents were analytically pure and used without further purification. Commercial melamine (A.R. ≥98%) and ethanol (99.7%) were purchased from Aladdin Corporation and Tianjin Fuyu Fine Chemical Co. Ltd., respectively. Ultrapure water was used in the all experiments.

2.2 Synthesis of g-C_3N_4 samples

The synthesis process of porous O-doped g-C_3N_4 nanosheets (denoted as POCN) was as follows: commercial melamine powder (5 g) and ethanol (0.75 mL) were added into 60 mL ultrapure water and stirred for 10 min. Then, the mixture was transferred into a 100 mL Teflon-lined stainless autoclave and kept at 200 °C for 6 h. After cooling to room temperature naturally, the suspension was separated by centrifugation, washed with ultrapure water and ethanol several times, and then dried at 60 °C for 12 h to obtain the modified precursor. Finally, this modified precursor (2 g) was calcined at 550 °C for 2 h in a muffle furnace at a heating rate of 0.5 °C min^{-1} under an air atmosphere. After cooling to room temperature naturally, the as-prepared POCN product was obtained. For comparison, the other samples were prepared with the same experimental process as mentioned above by varying the volume of ethanol (0, 0.25, 0.50 and 1.00 mL) in the hydrothermal step, and marked as HCN, POCN-0.25, POCN-0.50 and POCN-1.00, respectively. Moreover, the bulk g-C_3N_4 (denoted as CN) was prepared by directly heating the commercial melamine (2 g) in a muffle furnace at 550 °C for 2 h at a heating rate of 0.5 °C min^{-1} under an air atmosphere.

2.3 Characterization

The crystal structure of g-C_3N_4 was characterized by powder X-ray diffraction (XRD) with a Cu Kα_1 radiation source (40 kV/40 mA). The functional groups were characterized by Fourier transform infrared (FTIR) spectroscopy on a Bruker Tensor 27 spectrometer instrument. The microstructure and morphology were determined by transmission electron microscopy (TEM, JEOL JEM-2100) at 200 kV. The UV-vis diffuse reflectance spectrum (UV-vis DRS) was obtained using a UV/vis/NIR spectrophotometer (Hitachi U-4100) with $BaSO_4$ as the reflectance standard. The chemical composition and surface state were examined by X-ray photoelectron spectroscopy (XPS, Thermo ESCALAB Xi+) with a monochromatized Al Kα line source (200 W). The Brunauer–Emmett–Teller (BET) specific surface area was surveyed by the nitrogen adsorption–desorption method at 77 K on a Quantachrome apparatus. The pore size distribution was obtained by using a Barrett–Joyner–Halenda (BJH) model. The room-temperature photoluminescence (PL) spectrum was measured by using a fluorescence spectrophotometer (Dong Woo Optron) with an excitation wavelength of 325 nm at room temperature. In addition, thermogravimetric analysis (TGA) was performed on a NETZSCH STA449F3 instrument under a flow of nitrogen at a heating rate of 10 °C min^{-1}. Solid-state ^{13}C magic angle spinning (MAS) NMR measurement was conducted on a Bruker AVANCE III 400 MHz WB solid-state NMR spectrometer at room temperature.

2.4 Photocurrent measurement

A photocurrent test was performed on an electrochemical workstation (CHI660E, Chenhua Instruments, Shanghai) in a quartz cell of a three-electrode system, including a Pt counter electrode, an Ag/AgCl reference electrode and a working electrode. The working electrode was prepared as follows: 10 mg sample was added into 1.0 mL ultrapure water and 20 μL Nafion with ultrasonic dispersion for 1 h to form a uniform slurry. Then, the above slurry was coated smoothly on a 2 × 2 cm fluorine-doped tin oxide (FTO) glass with a deposit area of 1 cm^2. Finally, after being dried at 60 °C for 12 h, the FTO glass deposited with the sample was annealed at 300 °C for 2 h in a muffle furnace to obtain the working electrode. The electrolyte was a 0.5 M Na_2SO_4 aqueous solution (60 mL), and the light source was a 300 W Xe lamp ($\lambda > 420$ nm).

2.5 Photocatalytic hydrogen evolution

Photocatalytic hydrogen evolution was performed using a LabSolar-IIIAG photocatalytic hydrogen generation system (Beijing Perfectlight Science & Technology Co., Ltd. China). The visible-light source was a 300 W Xe lamp equipped with a 420 nm cut-off filter. The reaction was accomplished in a 250 mL closed quartz reactor with a circulating water system. The specific experimental process was described as follows: initially, 50 mg of as-prepared photocatalyst was added into an aqueous solution, containing 90 mL ultrapure water and 10 mL triethanolamine (TEOA) as a scavenger, with ultrasonic dispersion for 15 min. Then, an appropriate amount of H_2PtCl_6 was added into the suspension and irradiated for 60 min to ensure that 1 wt% Pt was loaded on the photocatalyst surface. Afterwards, the photocatalytic hydrogen generation system was degassed for 30 min to remove air completely. Finally, the reaction suspension was irradiated for 3 h under visible light with a flow of cooling water (6 °C), and the evolved H_2 gas was analyzed by gas chromatography (GC7900, Tianmei, Shanghai) using a thermal conductivity detector at 30 min intervals.

Moreover, the apparent quantum efficiency (AQE) for hydrogen evolution was measured with the 300 W Xe lamp using band-pass filters with wavelengths of 420, 450, 475, 500 and 550 nm by using a similar procedure to that above. The AQE was calculated using the following equation:

$$\mathrm{AQE} = \frac{2 \times \text{amount of hydrogen evolution}}{\text{the number of incident photos}} \times 100\% \quad (1)$$

2.6 Computational parameters

First-principles calculations were performed using density functional theory (DFT) implemented in the Vienna *ab initio* simulation package (VASP).[18] The exchange–correlation energy was treated by the projected augmented wave (PAW) method with generalized gradient approximation (GGA) of Perdew, Burke, and Ernzerhof (PBE). Periodic boundary conditions that have a vacuum region with a length of 15 Å were adopted to ensure the cancellation of spurious interactions between periodic images. The energy cutoff and convergence criteria for energy and force were set to 500 eV, 10^{-4} eV, and 0.01 eV $Å^{-1}$. During the optimization procedure, 3 × 3 × 1 *K*-point was used, while 9 × 9 × 1 was applied for density of states (DOS) calculations. In addition, the most advanced hybrid functional (HSE06) was employed to calculate the electronic structures, because the PBE functional underestimates the bandgap of semiconductors.

3. Results and discussion

3.1 Synthetic strategy

A facile precursor molecule reforming strategy is developed here to construct POCN, which is a typical example of a purposefully designed and synthesized nanostructure. Schematic diagrams of the formation mechanisms of POCN and CN are shown in Fig. 1a. As shown in pathway I, CN was prepared by directly heating the commercial melamine under an air atmosphere. However, POCN can be synthesized by the thermal polymerization of functional melamine as shown in pathway II, which is described in two steps as follows. Firstly, the new hydroxylated and carbonylated melamine precursor was prepared by a hydrothermal ethanol-assisted precursor-reforming commercial melamine route. As shown in Scheme S1,† both ethanol and water molecules might play a key role in forming the hydroxyl (–OH) under hydrothermal conditions. Simultaneously, the acetaldehyde molecule resulting from the oxidized ethanol molecule might contribute to the formation of the carbonyl group (C═O).[19] As a result, the two functional groups (namely hydroxyl and carbonyl) are simultaneously anchored onto the edge of pristine melamine molecules. Secondly, POCN could be prepared by the thermal polymerization of the above functional melamine precursor, in which carbonyl groups might react with $–NH_2$ groups to form ═NH and the two hydroxyls (–OH) react to form C–O with the removal of water molecules (H_2O), respectively. As shown in Fig. 1b, it is seen that the anchored C═O group can react with the $–NH_2$ group to form a new ═NH group and H_2O, which is accompanied by the loss of oxygen atoms; thus these released oxygen atoms lead to the formation of a porous nanostructure (see the blue squares). Notably, the two anchored C–OH groups may react to construct a new C–O group with the removal of H_2O, which is attributed to the introduction of a heterogeneous oxygen atom into the final g-C_3N_4 framework (see the red squares). Because of the different functions of –OH and C═O groups, this reformed melamine can transform into porous O-doped g-C_3N_4 through the above thermal polymerization process.

As shown in Fig. S1,† the crystal structures of the POCN-precursor and HCN-precursor have remarkably changed after hydrothermal treatment, suggesting a phase transformation from the monoclinic phase to the orthorhombic phase, which has been demonstrated in previous studies.[9,20] In particular, compared with the HCN-precursor, the POCN-precursor not only undergoes a phase transition, but is also accompanied by the formation of new molecules through the introduction of ethanol during the hydrothermal process, and the new diffraction peaks are ascribed to the barbituric acid molecule (JCPDS No. 24-1553). Thus, it can be confirmed that the POCN-precursor consists of the barbituric acid molecule and orthorhombic-phase melamine, but the HCN-precursor is composed of just orthorhombic-phase melamine. The FTIR spectra of the different precursors are displayed in Fig. S2.† The broad peaks in the range of 3000–3600 cm^{-1} become slightly weak, suggesting that amino groups are partially substituted or broken.[17] The new peaks at 1778 cm^{-1} and 1707 cm^{-1} are attributed to the anhydride structure and C═O stretching vibration, respectively, indicating the formation of newly arranged molecular structures.[20,21] In addition, the sharp peak at 761 cm^{-1} further indicates that a portion of the triazine ring is changed due to the aromatic deformation of the ═C–H group.[22] In addition, the solid-state ^{13}C MAS

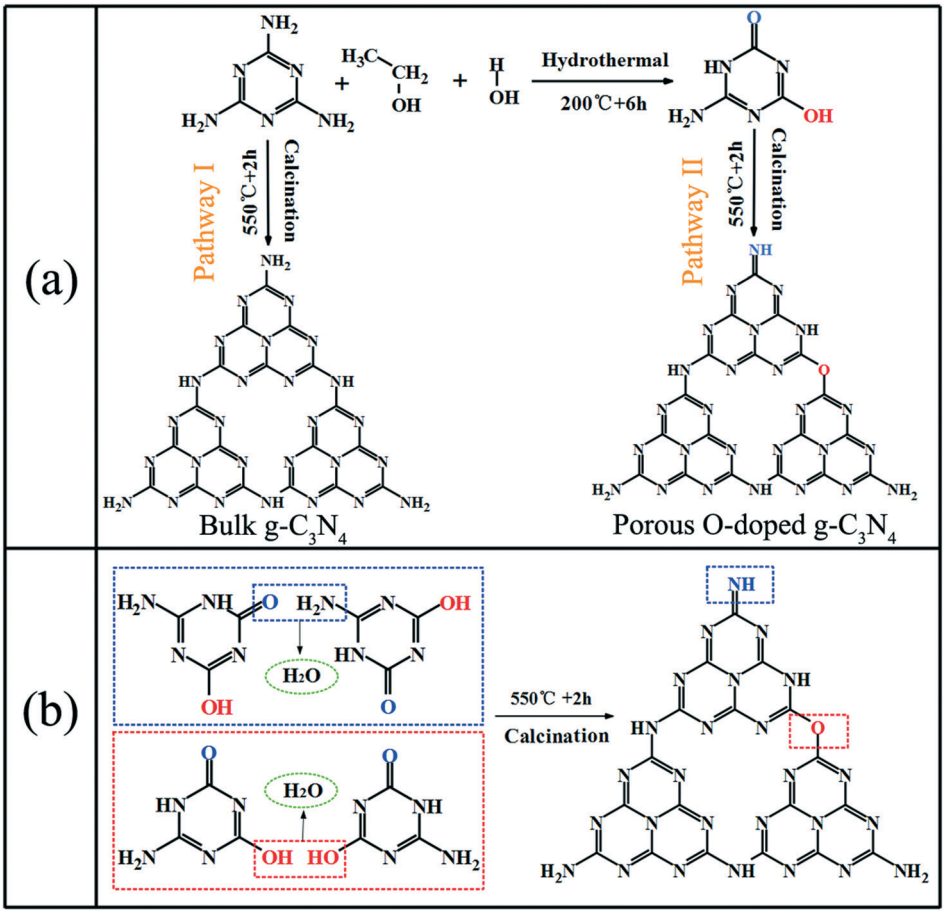

Fig. 1 (a) Schematic diagram of the formation mechanism of porous O-doped g-C_3N_4. (b) Thermal polymerization process for the one-pot synthesis of porous O-doped g-C_3N_4.

NMR spectra of the HCN-precursor and POCN-precursor are shown in Fig. S3.† It can be seen that the solid-state ^{13}C MAS NMR spectrum of the HCN-precursor shows only one peak originating from the intrinsic C–NH_2 of orthorhombic-phase melamine without the formation of a new molecule, which is consistent with previous studies (see Fig. S3a†).[9,23] However, the solid-state ^{13}C MAS NMR spectrum of the POCN-precursor displays three peaks at chemical shifts of 153.3, 161.7 and 167.6 ppm, which are assigned to C (1) atoms, C (2) atoms and C (3) atoms for the intrinsic C–NH_2, newly formed C═O group and newly formed C–OH group, respectively (see Fig. S3b†). Based on the above analysis, favorable evidence is provided to confirm that we have obtained the expected functional groups (including hydroxyl and carbonyl) in the reformed melamine, which is of great significance in explaining the formation mechanism of porous O-doped g-C_3N_4 nanosheets.

3.2 Morphology and microstructure

From the TEM images of the as-prepared samples, it can be seen that the CN sample shows a dense, stacked and non-porous characteristic bulk structure (see Fig. 2a). The HCN sample originating from the hydrothermally treated melamine displays a slight thinning compared with the CN sample (see Fig. 2b). In contrast, the POCN sample, whose precursor is the hydroxylated and carbonylated melamine, exhibits clear porous nanostructures and graphite-like nanosheets with wrinkled and almost transparent surface morphologies (Fig. 2c and d). Additionally, the N_2 adsorption–desorption isotherms of the three samples are presented in Fig. S4.† Obviously, the N_2 adsorption isotherm of POCN shows a representative type-IV curve with a typical H_3-type hysteresis loop, which demonstrates the presence of a mesoporous structure.[16] The BET specific surface area of POCN is 67.4 $m^2\ g^{-1}$, which is considerably higher than those of CN (14.0 $m^2\ g^{-1}$) and HCN (17.4 $m^2\ g^{-1}$). POCN shows two pore distribution centers at 3.37 nm and 28.6 nm, respectively (see Fig. S5†). Therefore, based on the above results, we can confirm that a mesoporous structure was formed for POCN, which will potentially benefit the improvement of the photocatalytic performance.

To investigate the formation mechanism of the mesoporous structure, TGA was employed to study the condensation process of POCN. As shown in Fig. S6,† all the precursors show a slight weight loss below 300 °C, which could be attributed to the evaporation of adsorbed molecules on the surfaces.[23,24] In the range of 300–450 °C, the weight of the three

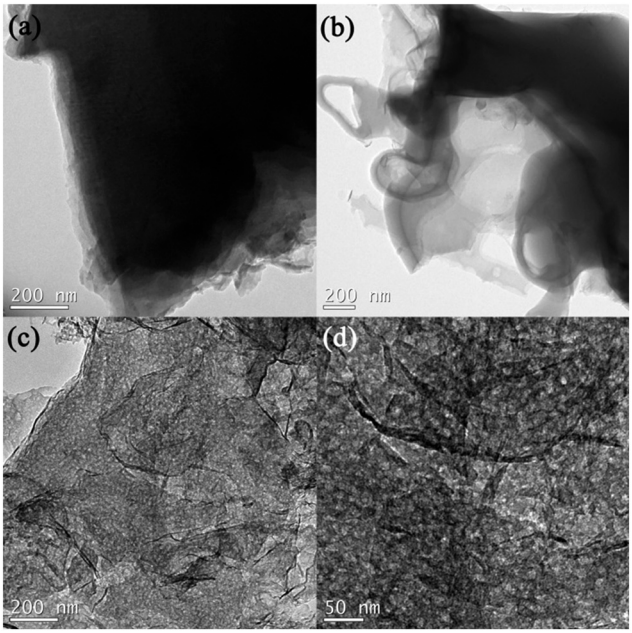

Fig. 2 TEM images of CN (a), HCN (b), and POCN ((c) and (d)).

precursors is dramatically reduced because of the intense thermal polymerization with the release of gases, such as NH_3, H_2O and so on. Hence, it can be inferred that the gas pressure would promote the formation of the mesoporous structure, and cause the breakage of π–π interaction of layers, reducing the stacking distance to achieve nanosheets.[24] When the calcination temperature is up to 550 °C, the TGA curves became relatively smooth, and the mass of the POCN-precursor, HCN-precursor and MA was 12.2, 27.7 and 31.2%, respectively. Thus, the precursor of POCN exhibited a higher mass loss and released more gas for producing more pores in the thermal polymerization process, finally leading to the formation of the mesoporous structure.

3.3 Crystal structure and chemical state

The crystal structure of the as-prepared samples was analyzed using XRD patterns (see Fig. 3a). The main diffraction peaks are observed at around 13.0° and 27.5°, which correspond to the (100) peak, derived from in-planar repeated *s*-triazine-based units, and the (002) interlayer-stacking peak, respectively, suggesting the formation of a graphitic-like structure.[25] However, the (100) and (002) peaks for POCN are apparently weaker compared with those of CN, which could result from in-plane porous structures and the reduced stacking distance between the g-C_3N_4 interlayers. In particular, the (002) peak shows a slight shift from 27.4° to 27.8°, which could be attributed to oxygen doping in the graphitic framework, leading to a shortened interplanar distance.[26,27] Moreover, the FTIR spectra of the three samples are similar (see Fig. 3b), indicating that the chemical structure is not changed. Typically, the absorption peak at 810 cm^{-1} is attributed to the breathing mode of the tri-*s*-triazine ring.[17,23,24] The peaks in the region

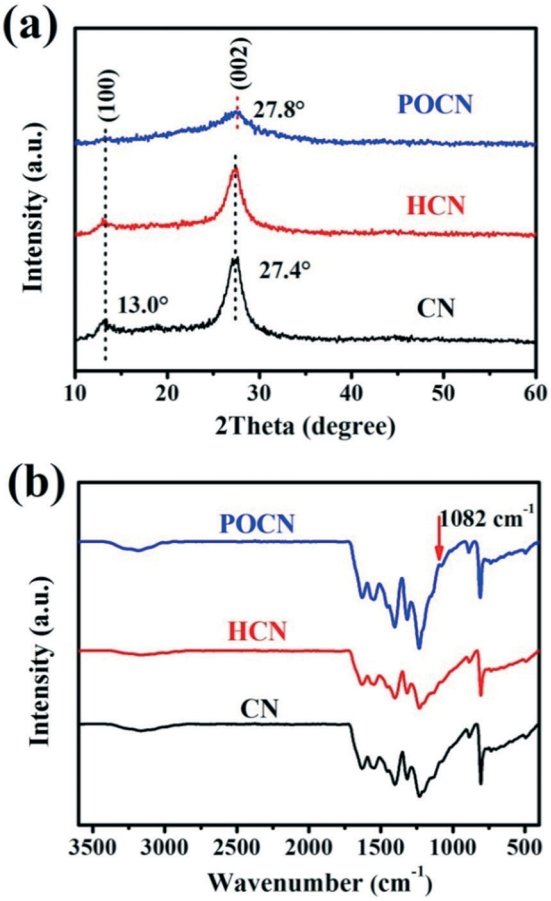

Fig. 3 (a) XRD patterns and (b) FTIR spectra of CN, HCN and POCN.

1200–1600 cm^{-1} are characteristic stretching modes of heptazine heterocyclic ring (C_6N_7) units.[17,23,24] In addition, the broad peaks ranging from 3000 to 3600 cm^{-1} are the stretching vibration modes of N–H.[17,23,24] Obviously, a new peak emerges at 1082 cm^{-1}, which is attributed to the C–O vibration in the g-C_3N_4 monolayer, suggesting the presence of an O-containing group in the POCN sample.[28]

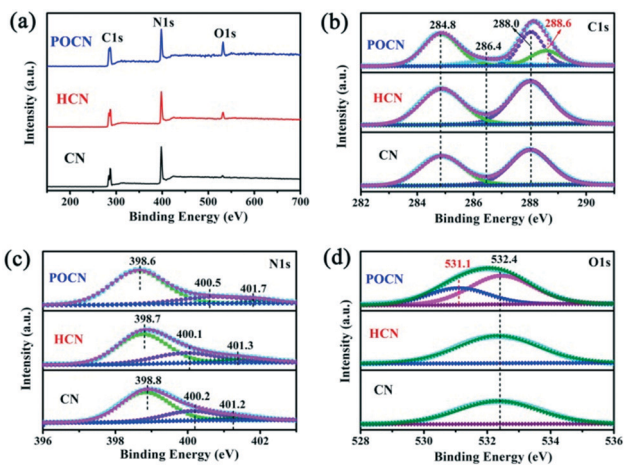

Fig. 4 (a) XPS survey spectra; (b)–(d) high-resolution C 1s, N 1s, and O 1s spectra of CN, HCN and POCN.

The XPS spectra were employed to further investigate the chemical bond states of CN, HCN and POCN, as shown in Fig. 4. The survey XPS spectra exhibit three peaks located at around 288, 398 and 532 eV, which are attributed to C 1s, N 1s and O 1s peaks, respectively (see Fig. 4a). It can be seen that the O 1s peak of POCN is much stronger than those of CN and HCN, suggesting that there is a higher content of O-containing species in the POCN sample.[15,28] In the high-resolution C 1s spectra (see Fig. 4b), all the samples display three peaks at 284.8, 286.6, and 288.0 eV, which are assigned to the C–C bonds in graphitic carbon species, C–NH_x (x = 1 and 2) on the edges of heptazine units, and N–C═N coordination in the framework of g-C_3N_4, respectively.[25,29–31] In particular, there is a new peak at 288.6 eV, suggesting the formation of C–O groups for POCN.[16] The high-resolution N 1s spectra (see Fig. 4c) could be fitted into three peaks centered at 398.6, 400.5 and 401.7 eV, which originate from the sp^2-hybridized nitrogen involved in the *s*-triazine rings (C–N═C), the inner N atoms bonded with three sp^3 carbon atoms (N–C_3), and the –NH_x groups, respectively.[25,29–31] The relative content of various nitrogen species of the three samples is listed in Table S1.† As expected, POCN possesses a decreased ratio of NH_x/(N–C_3) compared with the samples of CN and HCN, suggesting a larger polymerization degree, which is in agreement with the result of TGA. Moreover, a successive increase in the value of (C–N═C)/(N–C_3) is shown for CN, HCN and POCN. In particular, the value of POCN is almost 1.7 times that of CN, which can be attributed to the replacement of N–$(C)_3$ bonds with C–O bonds.[32] There is no clear XPS peak of the N–O bond at 402 eV, indicating that the oxygen atom is doped in the form of C–O bonds. In the high-resolution O 1s spectra (see Fig. 4d), the common peak of CN, HCN and POCN at 532.4 eV is assigned to the water on the surface, but POCN has an apparent new peak located at 531.1 eV corresponding to C–O.[16,28] Therefore, it can be demonstrated that the C–O bond is formed in the POCN sample. Moreover, the high-resolution O 1s spectra of POCN-0.25, POCN-0.50, and POCN-1.00 were investigated (see Fig. S7†). It can be seen that C–O peaks exhibit a progressive increase in intensity from POCN-0.25 to POCN-1.00, suggesting the increase of O-dopants, and the corresponding amount of O atoms is shown in Table S2.†

3.4 Optical and electronic properties

It is generally accepted that the optical properties and electronic band structure have a large effect on the photocatalytic performance. Thus, the UV-vis diffuse reflectance spectra (DRS) were used to investigate the optical absorption of the g-C_3N_4 samples. As shown in Fig. 5a, the optical

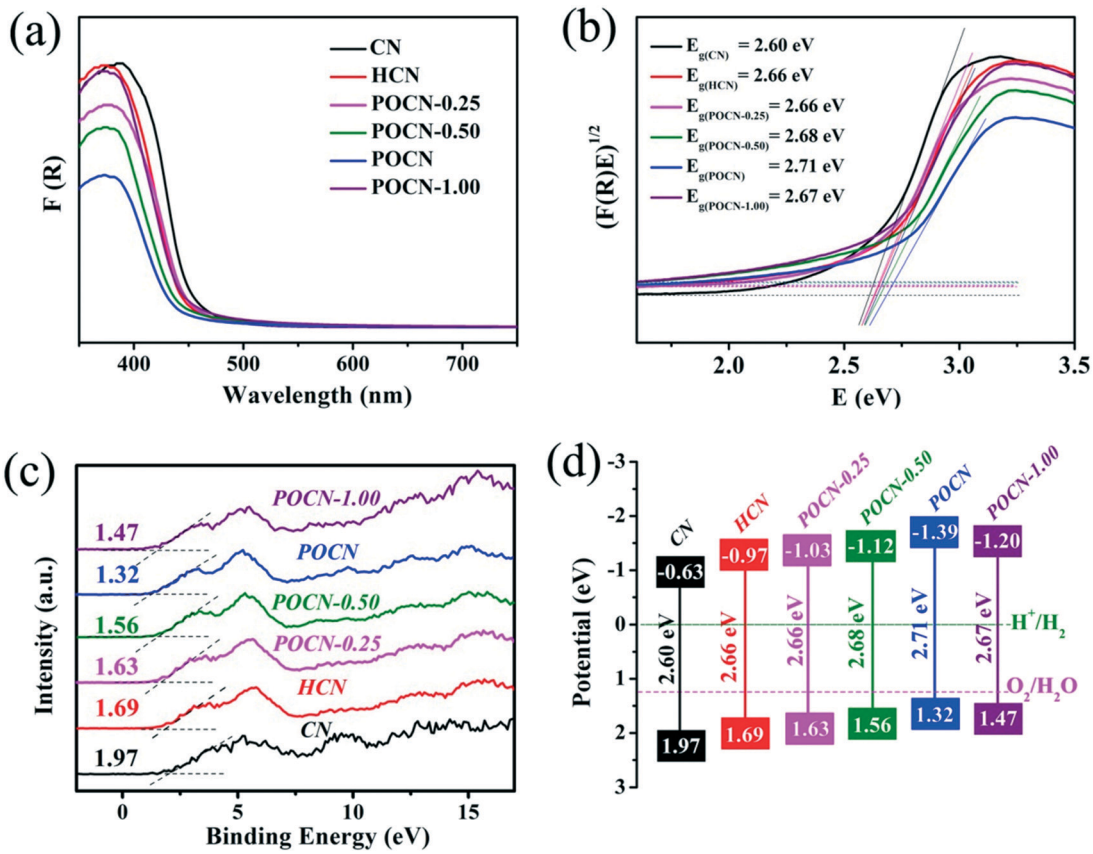

Fig. 5 (a) UV-vis DRS, (b) plots of transformed Kubelka–Munk function *versus* photon energy, (c) VB XPS spectra, and (d) band structure alignments of CN, HCN, POCN-0.25, POCN-0.50, POCN and POCN-1.00.

absorption spectra reveal that all the samples show intrinsic semiconductor-like absorption in the blue region of the visible spectra. In addition, among the modified samples, it is noted that the absorption edge of the POCN sample exhibits the most obvious blue-shift compared with CN, which could be ascribed to the quantum confinement effect (see Fig. 5a).[24,33] The bandgap energies of all the samples are derived by the Kubelka–Munk method. Correspondingly, the bandgap of CN, HCN, POCN-0.25, POCN-0.50, POCN and POCN-1.00 is determined to be 2.60, 2.66, 2.66, 2.68, 2.71 and 2.67 eV, respectively (see Fig. 5b). Moreover, to further obtain the energy band structure, the VB edges of the above-mentioned samples were investigated by valence band XPS (VB-XPS). As shown in Fig. 5c, the VB maximum (VBM) potentials of CN, HCN, POCN-0.25, POCN-0.50, POCN and POCN-1.00 are 1.97, 1.69, 1.63, 1.56, 1.32 and 1.47 eV, respectively. Combining the results of Kubelka–Munk plots,[34,35] the corresponding conduction band minimum (CBM) potentials of CN, HCN, POCN-0.25, POCN-0.50, POCN and POCN-1.00 are calculated to be −0.63, −0.97, −1.03, −1.12, −1.39 and −1.20 eV, respectively. Based on the above results, the energy band structure of the samples can be described in Fig. 5d. It should be noted that all the samples satisfy the thermodynamic conditions for photocatalytic hydrogen evolution, and the conduction band energy of POCN-0.25, POCN-0.50, POCN and POCN-1.00 is upshifted, indicating the enhancement of photoreduction ability. In particular, the CBM of POCN is calculated to be remarkably up-shifted by 0.76 eV and 0.42 eV compared with that of CN and HCN, which is beneficial to the enhancement of the photocatalytic hydrogen evolution performance due to the increased reduction driving force.[36,37] DFT calculations were conducted to illustrate the optimized electronic structure. The geometry structure of O-doped g-C_3N_4 is presented in Fig. S8a.† The DOS for relaxed structures of pristine g-C_3N_4 and O-doped g-C_3N_4 was calculated using the HSE06 functional, and the VBM of pristine g-C_3N_4 is chosen as the Fermi energy, and is set to zero. As shown in Fig. S8b,† DOS calculation results suggest that the doping peak of O-doped g-C_3N_4 is below the bottom of the CB, suggesting a typical n-type behavior. Moreover, a narrowing of the band gap for O-doped g-C_3N_4 (2.55 eV) compared with pristine g-C_3N_4 (2.72 eV) is shown, which is distinct from the experimental values. The distinction between DFT and experimental values can be rationalized by the quantum confinement effect, which results in the opposite shifting of the VB and CB edges, corresponding to the previous literature.[15]

Moreover, PL spectroscopy and photocurrent response measurements were performed to investigate the charge carrier behaviors, including the charge separation, migration, and recombination of photogenerated electron–hole pairs. As shown in Fig. 6a, the PL results demonstrate that POCN-0.25, POCN-0.50, POCN and POCN-1.00 all have a weak emission peak in contrast to the strong emission peak exhibited by CN and HCN, suggesting that the recombination rate of photoreduced electron–hole pairs is efficiently restrained.[38] Notably, along with the increase of O-dopants, there is a progressive decrease

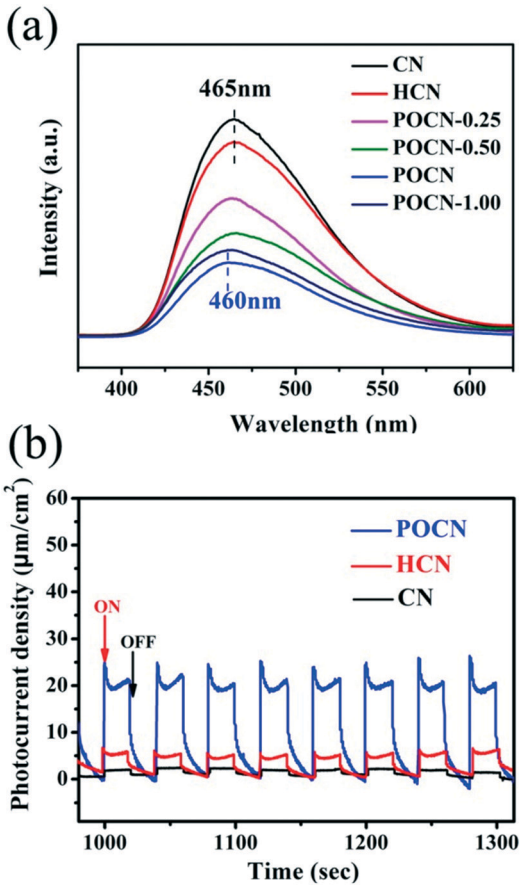

Fig. 6 (a) PL spectra and (b) transient photocurrent responses of CN, HCN and POCN.

in intensity of the emission peak, but POCN presents the weakest emission peak intensity rather than POCN-1.00. So the appropriate amount of O-dopants is very important for limiting the recombination of charge carriers, and excessive O-dopants seem to form defect sites that act as electron–hole recombination centers, resulting in the decreased photocatalytic efficiency, as reported in previous studies.[15,32] Furthermore, it can be found that the PL spectra of the O-doped samples, especially POCN, show obvious blue shifts, which might be caused by the quantum confinement effect.[28] Additionally, the photocurrent response is measured to further study the charge transport efficiency of CN, HCN and POCN by repeated use in eight on–off cycles under intermittent visible light irradiation ($\lambda > 420$ nm). As shown in Fig. 6b, POCN displays the highest photocurrent intensity compared with HCN and CN, indicating the improved transport of charge carriers.[39] Therefore, the above test results illustrate that the charge carrier behavior of POCN is significantly optimized. The enhanced charge separation and migration efficiency help to understand the enhanced photocatalytic activity.

4. Photocatalytic performance

The photocatalytic performance of the as-prepared samples was evaluated by hydrogen evolution, which was conducted

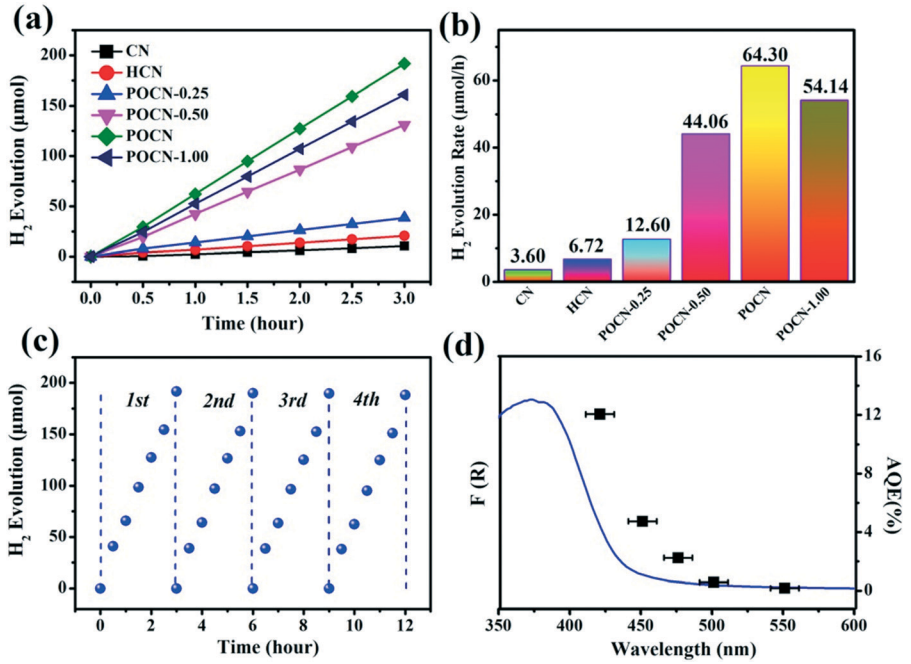

Fig. 7 (a) Time course of the HER over 3 h for the as-investigated samples (50 mg) in an aqueous solution containing 10 vol% TEOA added with 1 wt% Pt (H_2PtCl_6) under visible light irradiation. (b) The corresponding HER values. (c) The recycling performance of the POCN sample. (d) The AQE of the POCN sample.

by irradiating 100 mL of solution containing 10% volume of triethanolamine (TEOA) as a hole scavenger and 1 wt% Pt as a co-catalyst under visible light ($\lambda > 420$ nm). As shown in Fig. 7a, the as-prepared O-doped samples, including POCN-0.25, POCN-0.50, POCN and POCN-1.00, all exhibit increased photocatalytic hydrogen production compared with CN and HCN. The average hydrogen evolution rate (HER) of POCN-0.25, POCN-0.50 and POCN-1.00 is 12.60, 44.06 and 54.14 μmol h^{-1}, and in particular, the HER of POCN reaches a maximum (64.30 μmol h^{-1}), which is 17.8 times higher than that of CN (3.60 μmol h^{-1}) (see Fig. 7b). However, it is noted that POCN-1.00 shows a lower HER than POCN, which results

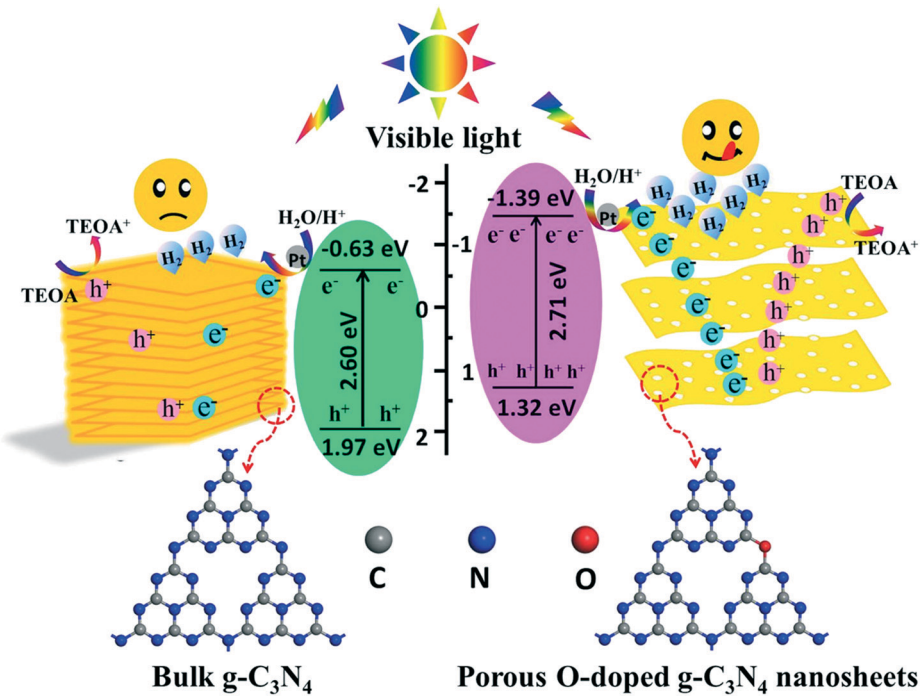

Fig. 8 Schematic diagram of the photocatalytic enhancement mechanism of POCN.

from the excess O-dopants forming more defect sites that act as electron–hole recombination centers, leading to the decreased charge separation efficiency (as shown in PL results).[15] The cycling result indicates that the HER of POCN has no apparent attenuation after four cycles (see Fig. 7c). Meanwhile, to explore the details of visible-light-driven activity for hydrogen evolution, the AQE was estimated at different wavelengths, as shown in Fig. 7d. The trend of hydrogen production matches exactly with the optical absorption of POCN, implying that the hydrogen production reaction is indeed induced by the photocatalytic excitation of the nanosheets.[40,41] The calculated AQE of POCN can reach 12.06% at 420 nm. The chemical and photochemical stabilities of a catalyst are key considerations for practical applications.[9,42] From the TEM, XRD and FTIR patterns of the recycled POCN, we can also find that there is no significant change in the microstructure, phase and chemical structure, respectively, indicating the excellent chemical stability of the POCN sample (Fig. S9–S11†). Moreover, the photocatalytic activities of modified g-C_3N_4 reported in previous studies are shown in Table S3,† indicating that the as-synthesized POCN shows a relatively improved photocatalytic performance, including the HER and AQE.

The probable photocatalytic mechanism of hydrogen evolution from water splitting and the schematic of the remarkably improved photocatalytic activity are illustrated in Fig. 8. Under the excitation of visible light, the photo-generated electrons transfer to the surface of the samples, and couple with ultrathin Pt nanoparticles. The hydrogen ions accept coupled-Pt electrons to produce hydrogen gas, while the holes react with TEOA through an oxidation reaction. In comparison with CN, the remarkably increased photocatalytic activity of POCN can be attributed to two factors. First, the mesoporous structure of POCN contributes to its high photocatalytic activity. POCN shows a large specific surface area of 67.4 m^2 g^{-1} and a pore size distribution of 28.6 nm in comparison with CN, which can provide more photocatalytically active sites, depress the recombination of photogenerated electrons and holes, improve the charge mobility, and promote the charge separation and migration from the interior to the surface.[15,17,22,24] Furthermore, O-doping can optimize the energy band structures. The appropriate amount of O-dopants in the graphitic structure can increase the electronic conductivity of POCN, which will promote the separation of charge carriers.[15] Meanwhile, the increased bandgap caused by the quantum confinement effect shifts the CBM potential of POCN to a more negative position according to the DFT results (see Fig. S8†), which can contribute to the stronger reduction capacity of electrons for hydrogen production.[28]

5. Conclusions

In summary, according to a purposefully designed precursor strategy, we have rationally constructed a new hydroxylated and carbonylated melamine precursor, which was an effective precursor for the synthesis of targeted porous O-doped g-C_3N_4 nanosheets (named as POCN) through a thermal polymerization method. The anchored hydroxyl on the edge of the melamine building block provided the heterogeneous oxygen atoms in the final g-C_3N_4, and the anchored carbonyl could be simultaneously removed in the form of water, leading to the formation of porous nanostructures due to the mass loss of functional melamine. Thus, the combination of exfoliation, porous nanostructure and oxygen doping was simultaneously achieved in the g-C_3N_4 framework. The as-obtained POCN possessed the advantages of a high specific surface area, increased reaction sites, and improved charge separation and transport efficiency. As a result, POCN showed remarkable improvement of photocatalytic hydrogen evolution performance. The HER of POCN was 64.30 μmol h^{-1}, which was 17.8 times higher than that of CN (3.60 μmol h^{-1}), and the AQE of POCN at 420 nm reached about 12.06%. This work demonstrated that the targeted g-C_3N_4 could be purposefully designed and prepared based on its formation mechanism, and would stimulate widespread investigations into the development of a designated precursor-reforming strategy for synthesizing highly-active g-C_3N_4 photocatalysts.

Conflicts of interest

There are no conflicts to declare.

Acknowledgements

This work was supported by the National Science Foundation of China (NSFC No. 51834009 and 51801151), the Hundred Talents Program of Shaanxi Province, the Key Laboratory Project of Shaanxi Education Department (No. 18JS070, 18JK0560 and 17JS081), the Shaanxi Province Science Fund for Distinguished Young Scholars (2018JC-027), China Postdoctoral Science Foundation (Grant No. 2018M633643XB), the Key Research and Development Project of Shaanxi Province (No. 2017ZDXM-GY-033 and 2017ZDXM-GY-028), and the Key Laboratory Project of Science and Technology Agency (No. 13JS075). In particular, the authors would like to dedicate this article to the 70th anniversary of the Xi'an University of Technology.

Notes and references

1 D. M. Schultz and T. P. Yoon, *Science*, 2014, **343**, 1239176.
2 G. G. Zhang, Z. A. Lan and X. C. Wang, *Angew. Chem., Int. Ed.*, 2016, **55**, 15712–15727.
3 X. Wang, X. Chen, A. Thomas, X. Fu and M. Antonietti, *Adv. Mater.*, 2009, **21**, 1609–1612.
4 G. Zhang, L. Lin, G. Li, Y. Zhang, A. Savateev, S. Zafeiratos, X. Wang and M. Antonietti, *Angew. Chem., Int. Ed.*, 2018, **57**, 9372–9376.
5 L. T. Ma, H. Q. Fan, M. M. Li, H. L. Tian, J. W. Fang and G. Z. Dong, *J. Mater. Chem. A*, 2015, **3**, 22404–22412.
6 Z. Lin and X. Wang, *Angew. Chem.*, 2013, **125**, 1779–1782.

7 J. Zhang, M. Zhang, R. Q. Sun and X. Wang, *Angew. Chem., Int. Ed.*, 2012, **51**, 10145–10149.
8 J. S. Zhang, Y. Chen and X. C. Wang, *Energy Environ. Sci.*, 2015, **8**, 3092–3108.
9 N. Tian, Y. H. Zhang, X. W. Li, K. Xiao, X. Du, F. Dong, G. I. N. Waterhouse, T. R. Zhang and H. W. Huang, *Nano Energy*, 2017, **38**, 72–81.
10 M. Arif, G. Yasin, M. Shakeel, M. A. Mushtaq, W. Ye, X. Y. Fang, S. F. Ji and D. P. Yan, *Mater. Chem. Front.*, 2019, **3**, 520–531.
11 Z. W. Zhao, Y. J. Sun and F. Dong, *Nanoscale*, 2015, **7**, 15–37.
12 H. B. Li, F. Y. Zhao, J. C. Zhang, L. Luo, X. J. Xiao, Y. C. Huang, H. B. Ji and Y. X. Tong, *Mater. Chem. Front.*, 2017, **1**, 338–342.
13 B. Lin, H. Li, H. An, W. B. Hao, J. J. Wei, Y. Z. Dai, C. S. Ma and G. D. Yang, *Appl. Catal., B*, 2018, **220**, 542–552.
14 B. Lin, G. D. Yang and L. Z. Wang, *Angew. Chem.*, 2019, **131**, 4635–4639.
15 Z. F. Huang, J. J. Song, L. Pan, Z. M. Wang, X. Q. Zhang, J. J. Zou, W. B. Mi, X. W. Zhang and L. Wang, *Nano Energy*, 2015, **12**, 646–656.
16 Y. B. Jiang, Z. Z. Sun, C. Tang, Y. X. Zhou, L. Zeng and L. M. Huang, *Appl. Catal., B*, 2019, **240**, 30–38.
17 C. Wang, H. Q. Fan, X. H. Ren, J. W. Ma, J. W. Fang and W. J. Wang, *ChemSusChem*, 2018, **11**, 700–708.
18 G. Kresse and J. Hafner, *Phys. Rev. B: Condens. Matter Mater. Phys.*, 1993, **47**, 558–561.
19 G. Garbarino, P. Riani, M. V. García, E. Finocchio, V. S. Escribano and G. Busca, *Catal. Today*, 2019, DOI: 10.1016/j.cattod.2019.01.002.
20 S. D. Sun, X. F. Gou, S. S. Tao, J. Cui, J. Li, Q. Yang, S. H. Liang and Z. M. Yang, *Mater. Chem. Front.*, 2019, **3**, 597–605.
21 A. I. Balabanovich, *Polym. Degrad. Stab.*, 2004, **84**, 451–458.
22 C. P. Marshall, E. J. Javaux, A. H. Knol and M. R. Walter, *Precambrian Res.*, 2005, **138**, 208–224.
23 S. D. Sun, J. Li, J. Cui, X. F. Gou, Q. Ying, S. H. Liang, Z. M. Yang and J. M. Zhang, *Inorg. Chem. Front.*, 2018, **5**, 1721–1727.
24 Y. T. Xiao, G. H. Tian, W. Li, Y. Xie, B. J. Jiang, C. G. Tian, D. Y. Zhao and H. G. Fu, *J. Am. Chem. Soc.*, 2019, **141**, 2508–2515.
25 H. J. Yu, R. Shi, Y. X. Zhao, T. Bian, Y. F. Zhao, C. Zhou, G. I. N. Waterhouse, L. Z. Wu, C. H. Tung and T. R. Zhang, *Adv. Mater.*, 2017, **29**, 1605148.
26 J. W. Fu, B. C. Zhu, C. J. Jiang, B. Cheng, W. You and J. G. Yu, *Small*, 2017, **13**, 1603938.
27 H. B. Fang, X. H. Zhang, J. J. Wu, N. Li, Y. Z. Zheng and X. Tao, *Appl. Catal., B*, 2018, **225**, 397–405.
28 X. J. She, J. J. Wu, J. Zhong, H. Xu, Y. C. Yang, R. Vajtai, J. Lou, Y. Liu, D. L. Du, H. M. Li and P. M. Ajayan, *Nano Energy*, 2016, **27**, 138–146.
29 J. J. Wu, N. Li, X. H. Zhang, H. B. Fang, Y. Z. Zheng and X. Tao, *Appl. Catal., B*, 2018, **226**, 61–70.
30 Y. B. Ding, Y. H. Tang, L. M. Yang, Y. X. Zeng, J. L. Yuan, T. Liu, S. Q. Zhang, C. B. Liu and S. L. Luo, *J. Mater. Chem. A*, 2016, **4**, 14307–14315.
31 L. Q. Yang, J. F. Huang, L. Shi, L. Y. Cao, Q. Yu, Y. N. Jie, J. Fei, H. B. Ouyang and J. H. Ye, *Appl. Catal., B*, 2017, **204**, 335–345.
32 J. H. Li, B. Shen, Z. H. Hong, B. Z. Lin, B. F. Gao and Y. L. Chen, *Chem. Commun.*, 2012, **48**, 12017–12019.
33 X. D. Zhang, X. Xie, H. Wang, J. J. Zhang, B. C. Pan and Y. Xie, *J. Am. Chem. Soc.*, 2013, **135**, 18–21.
34 J. R. Ran, T. Y. Ma, G. P. Gao, X. W. Du and S. Z. Qiao, *Energy Environ. Sci.*, 2015, **8**, 3708–3717.
35 H. M. Yaghoubi, Z. Li, Y. Chen, H. T. Ngo, V. R. Bhethanabotla, B. Joseph, S. Q. Ma, R. Schlaf and A. Takshi, *ACS Catal.*, 2015, **5**, 327–335.
36 W. N. Xing, C. M. Li, G. Chen, Z. H. Han, Y. S. Zhou, Y. D. Hu and Q. Q. Meng, *Appl. Catal., B*, 2017, **203**, 65–71.
37 D. Zhang, Y. L. Guo and Z. K. Zhao, *Appl. Catal., B*, 2018, **226**, 1–9.
38 L. J. Fang, X. L. Wang, J. J. Zhao, Y. H. Li, Y. L. Wang, X. L. Du, Z. F. He, H. D. Zeng and H. G. Yang, *Chem. Commun.*, 2016, **52**, 14408–14411.
39 S. L. Ma, S. H. Zhan, Y. N. Jia, Q. Shi and Q. X. Zhou, *Appl. Catal., B*, 2016, **186**, 77–87.
40 H. B. Tao, H. B. Yang, J. Z. Chen, J. W. Miao and B. Liu, *Beilstein J. Nanotechnol.*, 2014, **5**, 770–777.
41 L. T. Ma, H. H. Fan, J. Wang, Y. W. Zhao, H. L. Tian and G. Z. Dong, *Appl. Catal., B*, 2016, **190**, 93–102.
42 F. Y. Song, Y. Ding, B. C. Ma, C. L. Hill, C. M. Wang, Q. Wang, X. Q. Du, S. Fu and J. Song, *Energy Environ. Sci.*, 2013, **6**, 1170–1184.